Pol. J. Environ. Stud. Vol. XX, No. X (XXXX), 1-10
DOI: *10.15244/pjoes/215767* ONLINE PUBLICATION DATE: 2026-05-08

Original Research

Study on Attapulgite Loaded with Nano-Zerovalent Iron for Performance and Characterization

Ying Lv[1]°*, Xing Xue[2], Yuhang Peng[1], ZhanQiang Song[3], Dong Ma[1], Xiaolong Chen[1], Fuqiang Li[1], Ninghui Pan[1], Ding Wang[1], Run Chu[1]

[1]College of Resources and Environmental Sciences, Gansu Agricultural University, No. 1 Yingmen village, Anning District, Lanzhou 730070, Gansu, China
[2]Department of Anesthesiology, Jinshan Branch of Shanghai Sixth People's Hospital, Shanghai 201599, China
[3]Jingyuan County Bureau of Agriculture and Rural Affairs, Baiyin, Gansu, China

Received: 05 May 2025
Accepted: 17 December 2025

Abstract

This study focused on the synthesis and characterization of attapulgite loaded with nano-zerovalent iron (ATP-nZVI) nanocomposites, investigating their performance through systematic nanocomposite testing. The nanocomposites were prepared using attapulgite and various $FeCl_2$ concentrations, and the influence of $FeCl_2$ concentration was analyzed for their physicochemical properties and functional performance. ATP-nZVI nanocomposites were systematically characterized by X-ray diffraction, energy-dispersive X-ray spectroscopy, scanning electron microscopy, specific surface area, and a Fourier transform infrared spectrometer. The results showed that the optimal $FeCl_2$ concentration for ATP-nZVI nanocomposite synthesis was 0.10 g/mL. Detailed analysis revealed significant insights into how $FeCl_2$ concentration affected the crystal structure, surface morphology, porosity, functional groups of nanocomposites, and the distribution of nZVI on attapulgite. These findings provided important theoretical and practical guidance for optimizing synthesis parameters and improving the application efficiency of ATP-nZVI nanocomposites in environmental remediation and industrial processes.

Keywords: attapulgite, nano-zerovalent iron, nanocomposites, performance

Introduction

The increasing attention on nanocomposites composed of nano-zerovalent iron (nZVI) and clays is well-founded due to their unique combination of desirable properties [1]. These nanocomposites integrate the renewable and nontoxic characteristics of nZVI with the abundant, low-cost, heat-resistant, and reinforcing advantages of inorganic nanoclays [2]. The introduction of clays into nZVI-based nanocomposites significantly improves their mechanical properties, such as gel strength and resistance to deformation [3]. This is partly attributed to the interfacial interactions between nZVI particles and the clay layers, which can form a reinforcing network within the composite [4]. The clay component in these nanocomposites enhances their swelling ability and rate, which is crucial for applications in water treatment

*e-mail: conkly@163.com
°ORCID iD: 0000-0003-0269-3077

and soil remediation [5]. Additionally, the presence of clay improves the salt resistance of the composite, thereby increasing its durability and effectiveness in saline environments [6]. The large surface area of nZVI particles in contact with the clay matrix allows for efficient interaction and enhanced properties even with a small amount of filler [7]. This high contact area is beneficial for applications requiring high reactivity, such as environmental remediation and catalysis [8].

In the field of clay-based nanocomposites, the influence of clay on the properties of corresponding nanocomposite materials was investigated intensively. As the dominating member of the clay mineral family, attapulgite (ATP) is a typical crystalline hydrated magnesium silicate. Compared with other clay minerals, ATP is not only abundant in reserves and low-cost, but also features a highly porous structure. This structure is characterized by numerous internal nanoscale pores and grooves on its surface, which contribute to its large specific surface area. As a result, ATP exhibits exceptional adsorption, ion exchange, and catalytic properties. These characteristics render ATP a highly valuable component in clay-based nanocomposites, making it particularly valuable in agriculture, marine, and medical fields [9].

Given its many special physical and chemical properties, ATP has drawn much attention in the preparation of nano-zerovalent iron-attapulgite nanocomposites. These properties not only enhance the overall performance of the composite materials but also facilitate the development of new materials for specific applications [10]. These nanocomposites integrate the reactivity of nZVI with the stability and adsorption capacity of ATP [11]. ATP functions as a supporting medium to enhance the stability and dispersion of nZVI, thereby enhancing its reactivity while reducing its tendency to aggregate [12]. The development of such nanocomposites not only improves the individual properties of each component but also accelerates the creation of novel materials for special applications and advanced composite materials [13]. However, there is limited information available regarding how the physicochemical properties of clay influence the performance of nanocomposites. Therefore, further research is needed in this area. Meanwhile, the incorporation of ATP micropowder into the nano-zerovalent iron (nZVI) network has been shown to significantly enhance the comprehensive properties of these nanocomposites.

In this study, ATP was used as a material carrier to synthesize ATP-nZVI nanocomposites. The interaction between ATP and nZVI was evaluated, focusing on performance and characterization. The study aims to provide a comprehensive understanding of the ATP-nZVI nanocomposites by characterizing their physical and chemical properties and by evaluating the impact of $FeCl_2$ concentration on their performance and characterization. The results will help in optimizing the synthesis conditions and improving the application efficiency of ATP-supported nZVI in various environmental and industrial processes.

Materials and Methods

Preparation of the Polymer Sand-Fixing Material based on Attapulgite

According to Lv [14], a four-necked flask equipped with a mechanical stirrer, reflux condenser, thermometer, and nitrogen inlet was assembled and purged extensively with nitrogen to eliminate dissolved oxygen from the system. A mixture of acrylamide (7.1 g, dissolved in 20 mL distilled water) and H_2SO_4-modified attapulgite (0.71 g) was dispersed in a 250 mL four-necked flask under continuous stirring for 30 min. Subsequently, potassium persulfate (0.09 mg) and N,N'-methylene-bis-acrylamide (0.06 mg) were added as the initiator and crosslinker, respectively. The reaction mixture was allowed to polymerize in a water bath at 50ºC for 3 h. Finally, the synthesized polymer (8 g) was ground and treated with 40 mL of 1.5 mol/L NaOH. The mixture was gradually heated to 70ºC and maintained at this temperature for 2 h under continuous stirring. The resulting product was then thoroughly washed with distilled water to remove residual impurities and dried in an oven at 70ºC for 72 h.

Synthesis of Attapulgite Loaded with Nano-Zerovalent Iron

Initially, fumaric acid (1.0 g) was dissolved in 30 mL ethanol in a 60 mL glass vial with magnetic stirring. Subsequently, the attapulgite sample (1.0 g) was introduced into a separate 5 mL glass vial containing the prepared fumaric acid solution. The mixture was then dried at 50ºC in an oven. For the synthesis of attapulgite-loaded nano-zerovalent iron, the nanocomposites were produced through the reduction process of $FeCl_2$ with a $NaBH_4$ solution. Specifically, 0.01 g, 0.05 g, 0.1 g, 0.15 g, and 0.3 g of $FeCl_2$ powder were separately dissolved in 10 mL of deionized water in individual 20 mL glass vials under magnetic stirring. Each prepared $FeCl_2$ solution was then introduced to the dried attapulgite samples, followed by thorough homogenization. After mixing, the samples were dried again at 50ºC, ultimately yielding attapulgite-loaded nano-zerovalent iron composites with different iron loadings.

X-ray Diffraction (XRD)

XRD analysis was performed using a D/max III C-type X-ray diffractometer (Rigaku Corporation, Japan). The measurements were conducted over a 2θ range of 10° to 90° under the following experimental conditions: Cu Kα radiation (λ = 0.15406 nm) was generated by a copper anode X-ray tube operated at 40 kV and 300 mA. The data were collected with

a scanning step width of 0.05° at a scanning rate of 10°/min.

Energy Dispersive X-ray Spectroscopy (EDS)

The microstructure of the sample was characterized using a Gemini SEM300 SEM from Germany, equipped with an advanced X-MAX spectrometer manufactured by Oxford Instruments. This high-performance system offered a wide acceleration voltage range from 0.02 kV to 30 kV, achieving exceptional resolution capabilities of 1.2 nm at 1 kV and 0.7 nm at 15 kV. The instrument provided precise beam current control, adjustable from 3 pA to 20 nA, enabling detailed microstructural analysis across various experimental conditions.

Scanning Electron Microscopy (SEM)

The sample was first dispersed in ethanol via ultrasonication to ensure homogeneity. The suspension was then drop-cast onto a copper alloy substrate precoated with a conductive adhesive. After deposition, the sample was dried in an oven at 60ºC for 2 h to remove residual solvent. Finally, a thin gold layer was sputter-coated onto the sample surface to enhance conductivity prior to SEM analysis (SEM300, China).

BET Surface Area Analysis

The specific surface area and pore size distribution of the sample were characterized using nitrogen adsorption-desorption measurements performed on an Omnisorp 100CX Coulter analyzer (USA). Prior to analysis, the sample underwent degassing pretreatment at 573 K for 3 h under vacuum to remove physisorbed species from the surface. The Brunauer-Emmett-Teller (BET) method was employed to calculate the specific surface area from the adsorption branch of the isotherm. The pore volume and pore size distribution were derived from the desorption isotherm data using the Barrett-Joyner-Halenda (BJH) algorithm.

Fourier Transform Infrared Spectrometer (FTIR) Analysis

1-2 mg sample was placed into an agate mortar. It was ground into a fine powder and thoroughly mixed with dry potassium bromide powder. The mixture was transferred into a mold and pressed into a tablet using a tablet press. The tablet was compressed at a pressure of 10 MPa for 1 min. Finally, the tablet was removed from the mold and placed into an FTIR for scanning.

Results and Discussion

The performance and characterization of ATP loaded with nZVI can be thoroughly investigated through various analytical methods, including structural, porosity, functional group, and morphological properties. In recent years, a novel type of nanomaterial has been developed by functionalizing ATP and loading it with nZVI [15].

XRD of ATP-nZVI Nanocomposites

The XRD patterns of ATP loaded with varying concentrations of $FeCl_2$ were analyzed to elucidate the crystalline structure, phase composition, and particle size of nZVI loading. Typically, the XRD spectra displayed distinct peaks at specific 2θ angles, which corresponded to the crystallographic planes of nanocomposites, providing valuable insights into their structural characteristics [11]. The observed peaks are attributed to the crystallographic planes of the face-centered cubic structure in both functionalized attapulgite and ATP loaded with nZVI [16]. As shown in Fig. 1, the XRD peaks at 2θ = 26.9°, 28.2°, and 31.1° correspond to the (700), (158), and (113) planes of functionalized attapulgite (0 g/mL $FeCl_2$), respectively. The strongest diffraction peak of functionalized attapulgite (0 g/mL $FeCl_2$) appeared at 2θ = 26.9°, which was sharp and highly intense, serving as its characteristic diffraction peak. The results suggested that functionalized attapulgite possessed a complete crystalline structure. When 0.10 g/mL $FeCl_2$ was introduced onto ATP, the 2θ = 36.5° was observed in the spectrum of nZVI, which represented the successful loading of Fe^0. Similarly, the peaks at 30.9°, 50.3°, 36.9°, and 42.4° observed in the samples with 0.05 g/mL, 0.10 g/mL, 0.15 g/mL, and 0.30 g/mL $FeCl_2$ were representative of the successful loading of Fe^0. The characteristic diffraction peaks of ATP loaded with nZVI showed a decrease in intensity, while the position of the characteristic peaks remained largely unchanged, indicating that the structure of ATP-nZVI nanocomposites was not significantly altered. The results suggested that ATP-nZVI nanocomposites maintained a stable structure. Therefore, it was the concentration of $FeCl_2$ that significantly affected its XRD pattern characteristics [17]. These alterations may suggest variations in the crystalline structure resulting from the incorporation of nZVI onto the ATP framework [18]. By adjusting the concentration of $FeCl_2$, it was possible to control the crystal structure and particle size of nZVI, thereby optimizing its performance in critical applications such as environmental remediation [19, 20].

EDS of ATP-nZVI Nanocomposites

The EDS images provided comprehensive information about the distribution of various elements within the nanomaterial, which helped in understanding its composition and structure [21-23]. The EDS images illustrated the distribution of silicon (Si), oxygen (O), aluminum (Al), and iron (Fe) across different loading concentrations in Fig. 2. In the Si-EDS mapping, the distribution of Si was relatively uniform

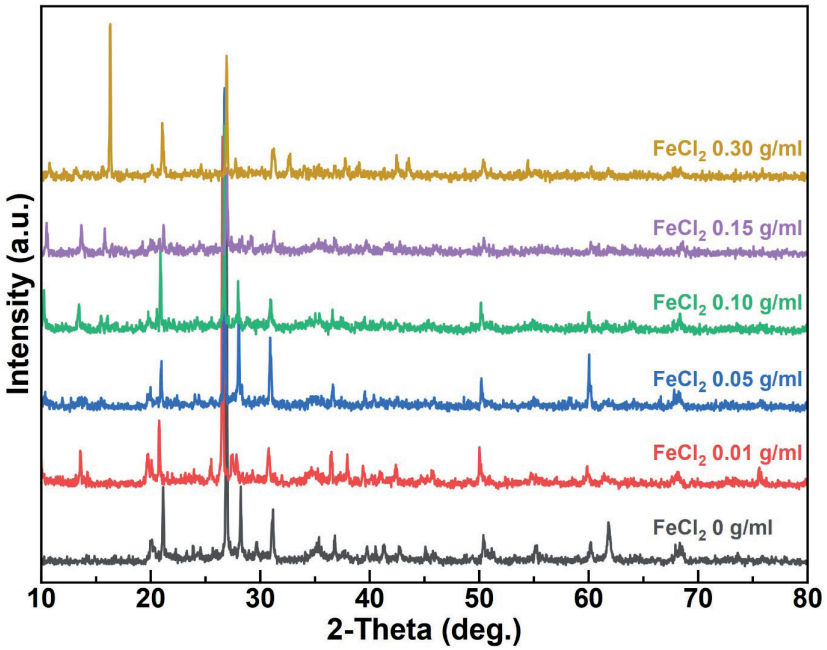

Fig. 1. XRD of attapulgite loaded with nano-zerovalent iron.

at all concentrations, and the number of blue dots increased significantly with increasing concentration; the distribution of Si was highlighted by a series of blue nanoparticles, clearly indicating the formation of a discrete Si phase. Similarly, in the O-EDS mapping, the distribution of O also became denser as the concentration increased; the presence of a discrete O phase was revealed by green nanoparticles. In the Al-EDS mapping, the distribution of Al was relatively uniform, but at higher concentrations (such as 0.30 g/mL), the distribution density increased significantly, and the formation of a discrete Al phase was shown by orange nanoparticles. For the Fe-EDS mapping, the presence of a discrete Fe phase was indicated by red nanoparticles; the distribution of Fe was relatively sparse in 0 g/mL $FeCl_2$, with the concentration of $FeCl_2$ solution increasing from 0.01 g/mL to 0.15 g/mL, the number of red dots increased and the distribution of Fe became more uniform, which represented the successful loading of Fe^0. However, in 0.30 g/mL $FeCl_2$, the distribution of Fe became dense, which represented an agglomeration of nZVI particles. The distribution of Si, O, and Al remained relatively stable across different concentrations, indicating that the intrinsic chemical composition of ATP was not significantly altered by varying nZVI loadings. Meanwhile, the increased and more uniform distribution of Fe at higher concentrations showed effective loading of nZVI onto the attapulgite. Therefore, the results showed that this uniform distribution of nZVI was crucial for enhancing the catalytic activity and reactivity of the nanocomposites. Specifically, a uniform and high concentration of nZVI loading could improve the adsorption and reduction capabilities of nanocomposites [24-26].

SEM of ATP-nZVI Nanocomposites

The SEM images revealed the morphological changes of ATP-nZVI treated with varying concentrations of $FeCl_2$ solution [13]. Fig. 3a) displayed functionalized attapulgite particles that possessed a relatively smooth surface and maintained intact shapes, indicating no significant nZVI deposition in the absence of $FeCl_2$. In Fig. 3b), the surface of the attapulgite particles was observed to begin showing small nZVI particles, although their distribution was not uniform. This indicated that Fe started to react with the attapulgite surface, resulting in the formation of a limited amount of nZVI at 0.01 g/mL $FeCl_2$ concentrations. The number and distribution of nZVI on the particle surface were observed to increase, and the surface became noticeably rougher in Fig. 3c). This indicated that 0.05 g/mL $FeCl_2$ concentration led to more Fe participating in the reaction, resulting in a greater amount of nZVI. The distribution of nZVI particles became more uniform, while the surface roughness also increased in Fig. 3d). This suggested that at this concentration, with an optimal range (around 0.10 g/mL), the reaction was more complete, leading to a higher loading of nZVI particles on the surface. The distribution of nZVI particles on the particle surface became denser, and the surface roughness was further enhanced, with more agglomerates forming in Fig. 3e). This might be due to the higher $FeCl_2$ concentration causing agglomeration of nZVI particles. The distribution of nZVI particles on the particle surface was extremely dense, and the surface appeared highly roughened, with significant agglomeration in Fig. 3f). This indicated that at this concentration, the loading of nZVI reached a high level, but agglomeration was also significant, potentially

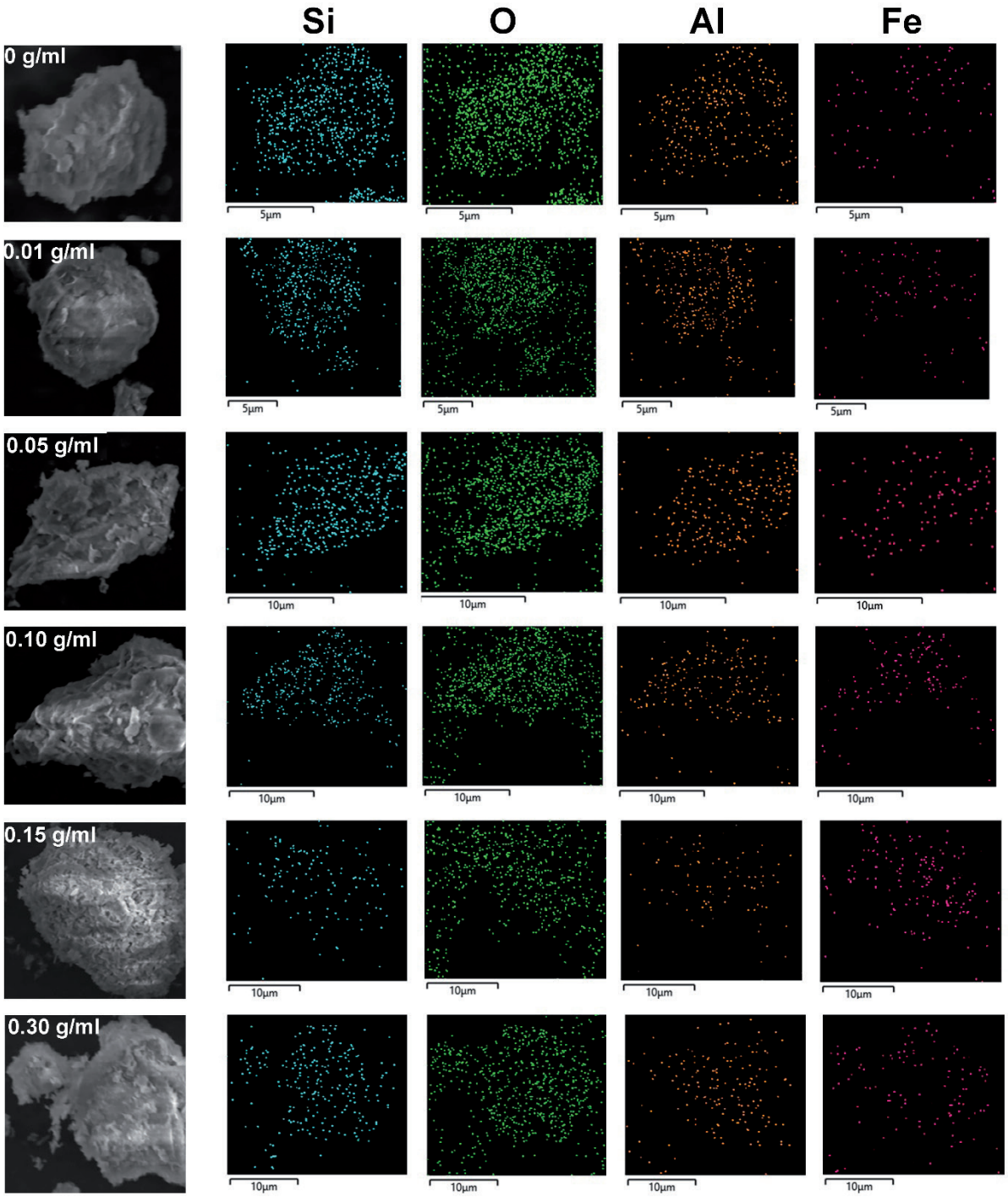

Fig. 2. EDS of attapulgite loaded with nano-zerovalent iron.

affecting its dispersion and reactivity. The results provided valuable insights into how the concentration of $FeCl_2$ influenced the surface characteristics and distribution of nZVI on attapulgite. As the $FeCl_2$ concentration increased from 0 g/mL to 0.30 g/mL, the quantity and distribution of nZVI particles on the attapulgite surface also increased, leading to a rougher surface. However, excessively high $FeCl_2$ concentrations could lead to significant agglomeration of nZVI particles, which might affect their dispersion and reactivity. Therefore, the concentration of 0.10 g/mL of $FeCl_2$ was identified as optimal for achieving the most effective loading of nZVI onto attapulgite.

Specific Surface Area of ATP-nZVI Nanocomposites

Specific surface area analysis was a crucial characterization technique used to accurately determine the specific surface area of materials. Widely employed across diverse fields such as porous materials, catalysts, adsorbents, and nanomaterials, it provided essential data

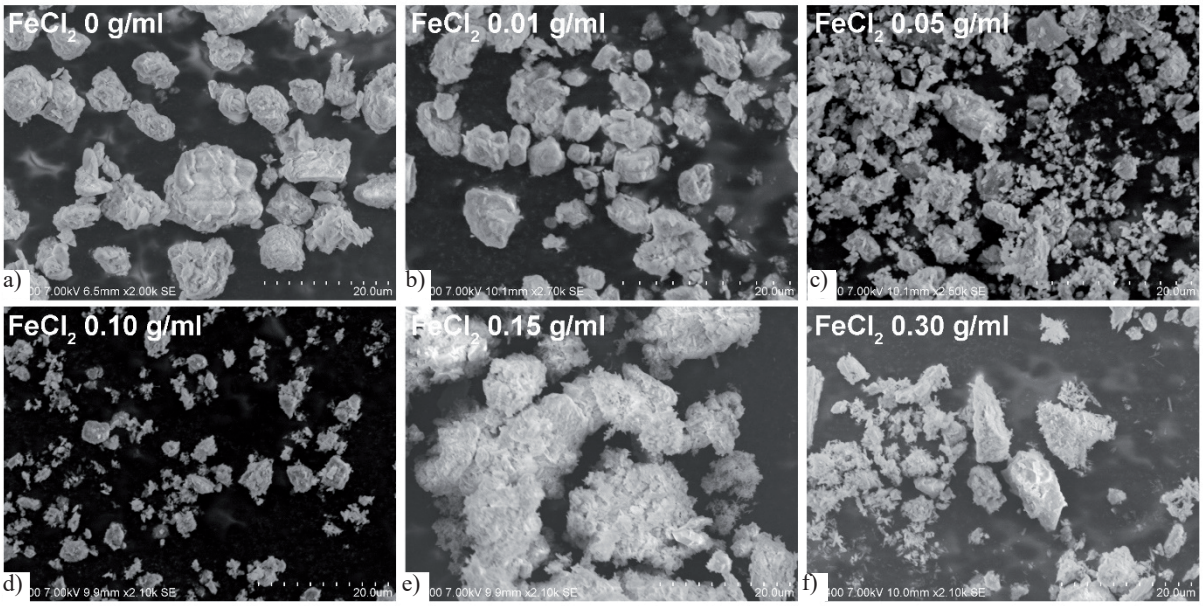

Fig. 3. SEM of attapulgite loaded with nano-zerovalent iron.

for investigating surface properties, pore structures, and adsorption performance [27]. By measuring a material's gas adsorption capacity, specific surface area analysis accurately reflected its surface characteristics [28]. Fig. 4 revealed a systematic trend in adsorption behavior with increasing $FeCl_2$ concentration. At low concentrations (0.01 g/mL and 0.05 g/mL), the adsorption capacity slightly improved, suggesting that trace amounts of $FeCl_2$ might enhance the material's specific surface area by introducing micropores or surface modifications. However, at higher concentrations (0.10 g/mL to 0.30 g/mL), the adsorption capacity significantly decreased, particularly for the 0.30 g/mL group, where the isotherm shifts downward markedly. This decline likely results from pore blockage or particle agglomeration caused by excessive $FeCl_2$, reducing accessible adsorption sites. As shown in Table 1, with $FeCl_2$ concentrations changing, S_{BET}, $V_{mic,}$ and D_{avg} of

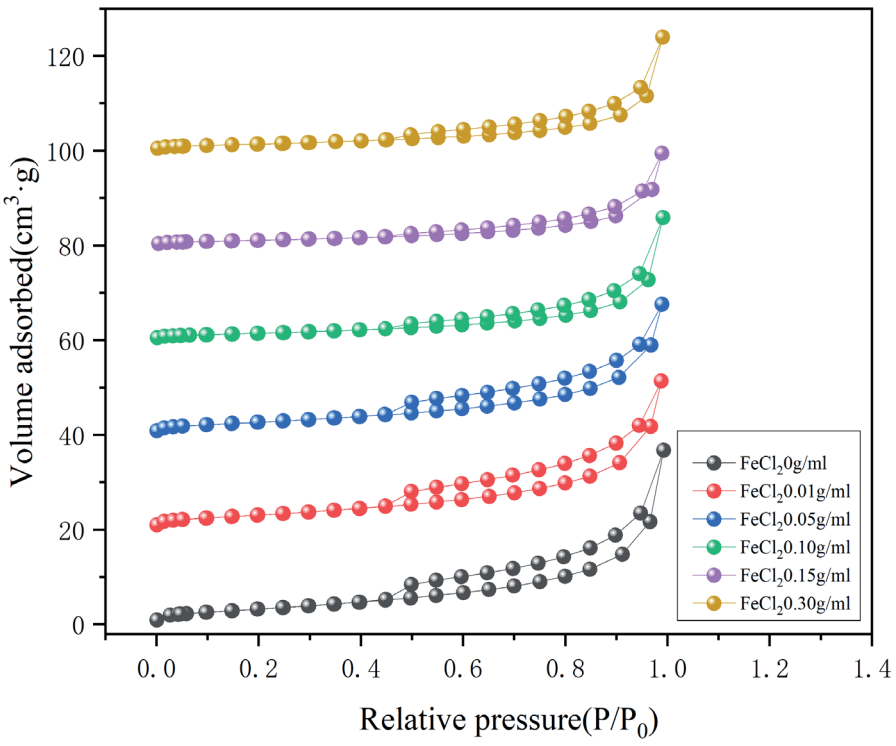

Fig. 4. Specific surface area of attapulgite loaded with nano-zerovalent iron.

Table 1. Specific surface area, pore volume, and average pore size of various materials.

	S_{BET} (m^2/g)	V_{mic}/(cm^3/g)	D_{avg}/(nm)
0g/mL $FeCl_2$	123.94	0.4000	18.33
0.01g/mL $FeCl_2$	117.17	0.4846	16.54
0.05g/mL $FeCl_2$	101.08	0.4261	16.86
0.10g/mL $FeCl_2$	135.46	0.5681	28.84
0.15g/mL $FeCl_2$	114.97	0.3008	28.66
0.30g/mL $FeCl_2$	115.13	0.3703	27.88

nanocomposites also changed. Among all concentrations, a dosage of 0.10 g/mL $FeCl_2$ simultaneously optimized both the specific surface area and the micropore volume, but was accompanied by a significant increase in pore size. The results showed that excessive irons, while enhancing the porous structure, lead to pore expansion. Overall, the effect of $FeCl_2$ concentration on the nanocomposite's pore structure was non-monotonic, with an optimal range (0.10 g/mL) for maximizing adsorption performance, while excessive concentrations degraded porosity. Additionally, a distinct hysteresis loop was observed in the mid-to-high pressure range, suggesting the formation of more mesoporous and macroporous structures and a significant enhancement in porosity. The sample without $FeCl_2$ (0 g/mL) demonstrated the lowest adsorption capacity, further confirming the role of $FeCl_2$ in modulating the nanocomposite's pore structure. A concentration of 0.10 g/mL was identified as optimal for promoting the formation of more mesoporous or macroporous structures and achieving a significant enhancement in porosity. Overall, the introduction of $FeCl_2$ had a profound impact on the nanocomposite's porous characteristics, likely by influencing pore-forming performance or crystal growth processes [29].

FTIR of ATP-nZVI Nanocomposites

FTIR was a powerful tool for analyzing the chemical structure of nanocomposites [30]. By analyzing the infrared spectra of ATP loaded with nZVI at various $FeCl_2$ concentrations, it was possible to provide important information about the chemical structure and functional groups of nanocomposites [31-33]. As shown in Fig. 5, the typical peak of Si-O-Si was located at 782 cm^{-1}, which showed that the basic structure of functionalized attapulgite (0 g/mL $FeCl_2$) remained intact. At 3609 cm^{-1}, the stretching vibrations of the C-OH peak were found, which possibly suggested the presence of hydroxyl groups or adsorbed water in functionalized attapulgite. At 2513 cm^{-1}, the stretching vibrations of the C≡N or C≡C peak were shown, which typically represented organic compounds in functionalized attapulgite. The bending vibrations of the O-H peak were located at 1434 cm^{-1}, indicating that functionalized attapulgite might contain adsorbed water or structural water. At 1347 cm^{-1} and 1578 cm^{-1}, the bending vibrations of the C-H peak and the stretching vibrations of the C=C peak were presented,

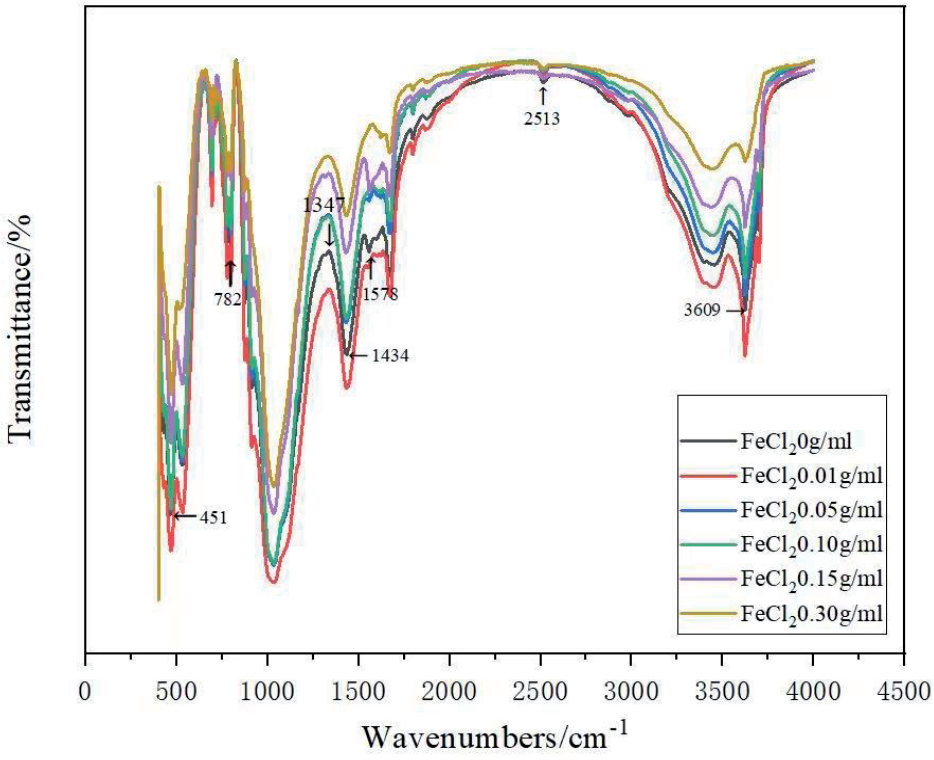

Fig. 5. FTIR of attapulgite loaded with nano-zerovalent iron.

which indicated the presence of organic impurities or functional groups in functionalized attapulgite. At 451 cm^{-1}, the peak was associated with the bending vibrations of Fe-O. Similarly, the FTIR spectrum of nanocomposites (0.01 g/mL $FeCl_2$) indicated diverse kinds of peaks were observed at 798, 3622, 2510, 1435, 1335, and 1557 cm^{-1}, corresponding to diverse modes of bonds, respectively. At 467 cm^{-1}, the stretching vibration peaks showed different degrees of shift compared with the peaks of functionalized attapulgite (0 g/mL $FeCl_2$); the result indicated that C-OH participated in the electron gain/loss process of Fe^{2+} or bonded with Fe^0 in the form of shared electrons. Therefore, the new absorption peak occurring at 467 cm^{-1} represented the successful loading of Fe^0. The bands at 797, 3621, 2512, 1433, 1343, and 1551 cm^{-1} corresponded to diverse peaks in 0.05 g/mL $FeCl_2$, and at 470 cm^{-1} the peak was associated with the bending vibrations of Fe^0, which represented the successful loading of Fe^0. The bands at 798, 3633, 2521, 1435, 1345, and 1578 cm^{-1} corresponded to diverse peaks in 0.10 g/mL $FeCl_2$, and at 471 cm^{-1} the peak was associated with the bending vibrations of Fe^0, which represented the successful loading of Fe^0. The bands at 798, 3629, 2513, 1429, 1344, and 1563 cm^{-1} corresponded to diverse peaks in 0.15 g/mL $FeCl_2$, and at 468 cm^{-1} the peak was associated with the bending vibrations of Fe^0, which represented the successful loading of Fe^0. The bands at 798, 3619, 2512, 1427, 1339, and 1570 cm^{-1} corresponded to diverse peaks in 0.30 g/mL $FeCl_2$, and at 471 cm^{-1} the peak was associated with the bending vibrations of Fe^0, which represented the successful loading of Fe^0. The results showed that the peak might become more pronounced with $FeCl_2$ concentration increasing, indicating the formation or enhancement of Fe-O and Fe^0 bonds, which demonstrated the successful loading of nZVI onto the attapulgite surface. Changes in this peak with increasing $FeCl_2$ concentration might indicate changes in the adsorption or desorption behavior of water molecules. The FTIR spectrum offered valuable insights into the structural and chemical property changes of ATP loaded with nZVI. By analyzing these characteristic peaks, a deeper understanding of the composition and properties of nanocomposites could be achieved, thereby providing a foundation for further application research [17, 34].

Conclusions

In summary, this study presented a comprehensive investigation into the synthesis and characterization of ATP loaded with nZVI, with a systematic evaluation of their performance through advanced nanocomposite testing techniques. The nanocomposites were synthesized using attapulgite and $FeCl_2$ at varying concentrations, with particular emphasis on elucidating the influence of $FeCl_2$ concentration on their physicochemical properties and functional performance. The XRD results indicated that ATP-nZVI nanocomposites maintained a stable structure because the concentration of $FeCl_2$ affected its XRD pattern characteristics. The EDS results suggested that the uniform distribution of nZVI was crucial for enhancing the catalytic activity and reactivity of the nanocomposites. The SEM results showed that the concentration of $FeCl_2$ influenced the surface characteristics and distribution of nZVI on attapulgite. The BET results showed that $FeCl_2$ concentration affected the porosity of ATP-nZVI. The FTIR results suggested that $FeCl_2$ concentration influenced the functional groups of nanocomposites. These findings provided important theoretical and practical guidance for optimizing synthesis parameters and improving the application efficiency of ATP-nZVI nanocomposites in environmental remediation and industrial processes. The thorough characterization and performance assessment conducted in this study not only deepened the understanding of ATP-nZVI nanocomposites but also highlighted their significant potential for various applications. This research contributed valuable insights to the field of nanocomposites and their practical implementation.

Acknowledgements

This research was supported by Gansu Province Key Research and Development Program for Ecological Civilization Construction (25YFFA020), the Natural Science Foundation of Gansu Province of China (23JRRA1592), Lanzhou Science and Technology Development Program-Science and Technology Major Project (2024-2-14), Science and Technology Plan Project of Gansu Province-Key Research and Development Program (25YFNA044), Major scientific and technological tasks of Gansu province-the central government to guide local science and technology development funds (25ZYJA032).

Conflict of Interest

The authors declare no conflict of interest.

Data Availability

Data will be made available on request.

References

1. ZHANG S.-Y., SHI H., ZHU M.-D., JIE W.-G., KAN L.-B. Synthesis, magnetic properties, biotoxicity and potential mechanism of modified nano zero-valent iron for decolorization of dye wastewater. Environmental Technology, **46** (2), 232, **2025**.
2. DI L., CHEN X., LU J., ZHOU Y., ZHOU Y. Removal of heavy metals in water using nano zero-valent

iron composites: A review. Journal of Water Process Engineering, **53**, 103913, **2023**.
3. YANG X., DAI X., JIAN T., TIAN W. Enhanced adsorption and reduction of Pb (II) from aqueous solution by sulfide-modified nanoscale zerovalent iron: characterization, kinetics and mechanisms. Inorganic Chemistry Communications, **170**, 113496, **2024**.
4. ZHONG X., LAI Y., WANG X., WANG M., HAN W., ZHANG M., JI H. Synthesis and environmental applications of biochar-supported nano-zero-valent iron composites: A review. Environmental Chemistry Letters, **22** (3), 1345, **2024**.
5. JAZZAR A., ALAMRI H., MALAJATI Y., MAHFOUZ R., BOUHRARA M., FIHRI A. Recent advances in the synthesis and applications of magnetic polymer nanocomposites. Journal of Industrial and Engineering Chemistry, **99**, 1, **2021**.
6. SARKAR T., KUNDU S., GHORAI G., SAHOO P.K., REDDY V.R., BHATTACHARJEE A. Structure, optical, magnetic, morphology and dielectric studies of pristine and green synthesized hematite nanoparticles. Applied Physics A, **130** (2), 123, **2024**.
7. WANG S., ZHAO M., ZHOU M., LI Y.C., WANG J., GAO B., SATO S., FENG K., YIN W., GALAVITHANA A.D., OLESZCZUK P., WANG X., OK Y.S. Biochar-supported nZVI (nZVI/BC) for contaminant removal from soil and water: a critical review. Journal of Hazardous Materials, **373**, 820, **2019**.
8. ZHANG X., CAO X.-Q., LI G., YIN J., ZHANG D., LI M., MENG N., DONG L., LYU X.-J., LI L., QIU J., ZHANG Y., WANG P., ZHANG Q.-J. Preparation of novel ALRCs/nZVI composite and its removal of Cr (VI) from aqueous. International Journal of Environmental Research, **14**, 123, **2020**.
9. BODUR B., BENLI A., BAYRAKTAR O.Y., ALCAN H.G., KAPLAN G., AYDIN A.C. Impact of attapulgite and basalt fiber additions on the performance of pumice-based foam concrete: mechanical, thermal, and durability properties. Archives of Civil and Mechanical Engineering, **25** (2), 74, **2025**.
10. MAITI S., GOEL S., DUTTA B.K. Synthesis, stabilization and characterization of zerovalent iron nanoparticles for remediation of hexavalent chromium–Comparing the hydrazine and sodium borohydride routes. Materials Science and Engineering: B, **314**, 118002, **2025**.
11. YANG Q., WANG H., ZHONG Y., LU G., DANG Z., ZHANG L. Co-adsorption behaviors and mechanisms of Cd (II), Pb (II), and Cr (VI) on sodium dodecyl sulfate modified attapulgite clay-supported nano zero-valent iron: Competitive or synergistic effect? Environmental Research, 121107, **2025**.
12. ZOU Y., WANG X., KHAN A., WANG P., LIU Y., ALSAEDI A., HAYAT T., WANG X. Environmental remediation and application of nanoscale zero-valent iron and its composites for the removal of heavy metal ions: a review. Environmental Science & Technology, **50** (14), 7290, **2016**.
13. ANANG E., HONG L., FAN X., ASAMOAH E.N. Attapulgite supported nanoscale zero-valent iron in wastewater treatment and groundwater remediation: synthesis, application, performance and limitation. Environmental Technology Reviews, **11** (1), 1, **2022**.
14. LV Y., FENG Y., LIU X. Study of the Physiological Characteristics of Didymodon vinealis with the Aid of Attapulgite-Based Nanocomposite. Polish Journal of Environmental Studies. **31** (5),4205, **2022**.
15. DUAN F., ZHU Y., LIU Y., WANG A. Fabrication of porous adsorbents from eco-friendly aqueous foam for high-efficient removal of cationic dyes and sustainable utilization assessment. Journal of Environmental Sciences, **137**, 395, **2024**.
16. BAGHERI M., JAFARI S.M., EIKANI M.H. Ultrasonic-assisted production of zero-valent iron-decorated graphene oxide/activated carbon nanocomposites: Chemical transformation and structural evolution. Materials Science and Engineering: C, **118**, 111362, **2021**.
17. XIE L., MA Q., CHEN Q., LIU Y., GUO P., ZHANG J., DUAN G., LIN A., ZHANG T., LI S. Efficient remediation of different concentrations of Cr-contaminated soils by nano zero-valent iron modified with carboxymethyl cellulose and biochar. Journal of Environmental Sciences, **147**, 474, **2025**.
18. MUKHERJEE R., KUMAR R., SINHA A., LAMA Y., SAHA A.K. A review on synthesis, characterization, and applications of nano zero valent iron (nZVI) for environmental remediation. Critical Reviews in Environmental Science and Technology, **46** (5), 443, **2016**.
19. SOLIEMANZADEH A., FEKRI M. The application of green tea extract to prepare bentonite-supported nanoscale zero-valent iron and its performance on removal of Cr (VI): Effect of relative parameters and soil experiments. Microporous and Mesoporous Materials, **239**, 60, **2017**.
20. LI Z., ZHU X., WEI X., ZHANG H., CAO N., SHI X., SUN B. Modified attapulgite loaded nanoscale zero-valent iron for Cr (VI) removal in three-dimensional electrode system: Performance and mechanism. Journal of Environmental Chemical Engineering, **13** (2), 115893, **2025**.
21. ZHANG M., DONG Y., GAO S., CAI P., DONG J. Effective stabilization and distribution of emulsified nanoscale zero-valent iron by xanthan for enhanced nitrobenzene removal. Chemosphere, **223**, 375, **2019**.
22. WEI Y., USMAN M., FAROOQ M., ADEEL M., HAIDER F.U., PAN Z., CHEN W., LIU H., CAI L. Removing hexavalent chromium by nano zero-valent iron loaded on attapulgite. Water, Air, & Soil Pollution, **233** (2), 48, **2022**.
23. ZHANG J., ZHAO X., WANG W., SONG Z., MAO Y., SUN J., CHEN S. Removal of p-nitrophenol by double-modified nanoscale zero-valent iron with biochar and sulfide: Key factors and mechanisms. Journal of Water Process Engineering, **51**, 103398, **2023**.
24. ZHANG Y., TAN Y., ZU B., ZHANG X., ZHENG C., LIN Z., HE F., CHEN K. Removal of nitrate nitrogen in groundwater by attapulgite loaded with nano-zero-valent iron. Adsorption Science & Technology, **2023**, 5594717, **2023**.
25. TESNIM D., DÍEZ A.M., AMOR H.B., SANROMÁN M.A., PAZOS M. Synthesis and characterization of eco-friendly cathodic electrodes incorporating nano Zero-Valent iron (NZVI) for the electro-fenton treatment of pharmaceutical wastewater. Chemical Engineering Journal, **502**, 158099, **2024**.
26. WEI S., HE C., ZHANG L., LI C., LI J., DU G. Advancements in removing common antibiotics from wastewater using nano zero valent iron. RSC Advances. **14** (36), 26272, **2024**.
27. WU X., ZHU Y., PEI B., CAI P., HUANG Z. Effect of $FeCl_2$ on the pore structure of porous carbon obtained from phenol formaldehyde resin and ethylene glycol. Materials Letters, **215**, 50, **2018**.
28. ZHENG Y., LV P., YANG J., XU G. Characterization and adsorption capacity of modified biochar for

sulfamethylimidine and methylene blue in water. ACS Omega, **8** (33), 29966, **2023**.
29. HOSNI Z., ACHOUR S., SAADI F., LIN J., SHENG J., AL QARAGHULI M. Specific surface area (SSA) of perovskites with uncertainty estimation approach. Computational Materials Science, **249**, 113668, **2025**.
30. KOTOV N., LARSSON P.A., JAIN K., ABITBOL T., CERNESCU A., WÅGBERG L., JOHNSON C.M. Elucidating the fine-scale structural morphology of nanocellulose by nano infrared spectroscopy. Carbohydrate Polymers, **302**, 120320, **2023**.
31. RAJ B., KALADHAR K. Nanomaterials for biomedical applications. In: Nanomedicine in Translational Research, p. 107, Elsevier, **2025**.
32. GE Z., CHEN X., FAN J. Efficient removal of harmful algae from eutrophic natural water by $Mg(OH)_2$ coated nanoscale zero-valent iron. Frontiers of Environmental Science & Engineering, **19** (4), 1, **2025**.
33. TULTABAYEVA T.C., CHOMANOV U.C., TULTABAYEV M.C., ZHUMALIYEVA G.E., KENENBAY G.S., SHOMAN A.Y., SHOMAN A.K. Synthesis, characterization and physical properties of polyunsaturated fatty acids and Co zero-valent nanoparticles/polyunsaturated fatty acids. Journal of Nanostructures, **12** (4), 1049, **2022**.
34. BAHÇELI S., SARıKAYA E.K., DERELI Ö. Photovoltaic performance of 4-Cyano-3-fluorobenzaldehyde: spectroscopic (FT-IR, 1H and 13C-NMR, FT-Raman, and UV–vis.) and DFT studies. Research on Chemical Intermediates, **51** (5), 2645, **2025**.